A Unified Description of Non-Radiative Voltage Losses in Organic Solar Cells

Xian-Kai Chen[1,†], Deping Qian[2,†,*], Yuming Wang[2], Thomas Kirchartz[3,4], Wolfgang Tress[5], Huifeng Yao[6], Jun Yuan[2,7], Markus Hülsbeck[3], Maojie Zhang[8], Yingping Zou[7], Yanming Sun[9], Yongfang Li[6,8], Jianhui Hou[6], Olle Inganäs[2], Veaceslav Coropceanu[1,*], Jean-Luc Bredas[1,*], Feng Gao[2*]

1. Department of Chemistry and Biochemistry, The University of Arizona, Tucson, Arizona 85721-0088, United States.
2. Department of Physics, Chemistry and Biology (IFM), Linköping University, Linköping 58183, Sweden
3. IEK5-Photovoltaik, Forschungszentrum Jülich, 52425 Jülich, Germany
4. Faculty of Engineering and CENIDE, University of Duisburg-Essen, Carl-Benz-Str. 199, 47057 Duisburg, Germany
5. Institute of Computational Physics, Zurich University of Applied Sciences, Wildbachstr. 21, 8401 Winterthur, Switzerland
6. Beijing National Laboratory for Molecular Sciences, Institute of Chemistry, Chinese Academy of Sciences, Beijing 100190, China.
7. College of Chemistry and Chemical Engineering, Central South University, Changsha 410083, China
8. Laboratory of Advanced Optoelectronic Materials, College of Chemistry, Chemical Engineering and Materials Science, Soochow University, Suzhou 215123, China
9. School of Chemistry, Beihang University, Beijing 100191, China

† These authors contributed equally.

* Correspondence to: deping.qian@liu.se (D.Q.); coropceanu@arizona.edu (V.C.); jlbredas@arizona.edu (J.L.B.); feng.gao@liu.se (F.G.)

Abstract:

Recent advances in organic solar cells (OSCs) based on non-fullerene acceptors (NFAs) come along with reduced non-radiative voltage losses ΔV_{nr}. We show here that, in stark contrast to the energy-gap-law dependence observed in conventional fullerene-based blends, the ΔV_{nr} values in these state-of-the-art NFA-based blends do not correlate with the energies of charge-transfer electronic states at donor:acceptor interfaces. Firmly based on combined temperature-dependent electroluminescence experiments and dynamic vibronic simulations, we provide a unified description of ΔV_{nr} for both fullerene- and NFA-based devices, and highlight the critical role of the thermal population of local exciton states –a feature commonly neglected– in the low ΔV_{nr} values of OSCs. A critical finding of our work is that the molecular photoluminescence properties of the pristine materials define the upper limit of the open-circuit voltage in OSCs, indicating that it is critical to design high-luminescence-efficiency donor and acceptor materials with complementary optical absorption bands extending into the near-infrared region. We also demonstrate that the reduction in ΔV_{nr} (*e.g.*, < 0.2 V) can be obtained without sacrificing charge-generation efficiency, providing a clear guidance for the rational design of next-generation, high-efficiency OSC blends.

Main Text:

Over the past five years, the power conversion efficiencies (PCEs) of single heterojunction organic solar cells (OSCs) have jumped from 11% to 18%, [1-2] increasingly closing the gap with inorganic and hybrid semiconductor solar cells. One of the breakthroughs accounting for the rapid progress in OSC PCEs is the significant reduction in voltage losses. [3-6] In particular, major efforts have focused on reducing the voltage losses due to non-radiative charge recombination (ΔV_{nr}) at donor:acceptor (D:A) interfaces. [6-15] However, the smallest ΔV_{nr} values of about 0.17 V currently achieved in high-efficiency OSCs [16] are still larger than those in inorganic devices (*e.g.*, ΔV_{nr} of 0.04 V in high-quality GaAs devices) [17-19].

The non-radiative voltage loss ΔV_{nr} is intrinsically linked to the external electroluminescence quantum efficiency (EQE_{EL}) of the device: [20]

$$\Delta V_{nr} = -\frac{k_B T}{e} \ln(EQE_{EL}) \quad (1)$$

where EQE_{EL} is related to both the radiative and non-radiative recombination rates (k_r and k_{nr}) of the D:A blend, *i.e.*, $EQE_{EL} \propto k_r/(k_r + k_{nr})$. An ideal EQE_{EL}=1 leads to $\Delta V_{nr} = 0$, while a reduction in EQE_{EL} by one order of magnitude increases the voltage loss by 58 mV at room temperature. The non-radiative decay rate k_{nr}^{CT} of the charge-transfer (CT) electronic state appearing at the D:A interfaces displays an exponential dependence (energy-gap law) as a function of CT-state energy (E_{CT}), *i.e.*, $k_{nr}^{CT} \propto \exp(-\beta E_{CT})$, where β is a constant. In D:A systems with CT-state energies in the near-infrared (NIR) region (where the optimal optical gaps for solar cells are situated), this can translate into an energy-gap law dependence of EQE_{EL} on E_{CT}, since $k_r^{CT} \ll k_{nr}^{CT}$ in the framework of the two-state model that involves exclusively the electronic CT and ground (G) states. [8] In that case, ΔV_{nr} is anticipated to display a linear dependence as a function of E_{CT}, *i.e.*, $\Delta V_{nr} = A - B \times E_{CT}$ (where A and B are constants); in fact, such a dependence was observed for fullerene-based blends. [8] Thus, ΔV_{nr} is expected to be especially large in D:A blends with low CT-state energies. Indeed, in fullerene-based blends that have optical absorption bands extending into the NIR region, the ΔV_{nr} values are usually above 0.3 V. [8] Within the two-state model, such large ΔV_{nr} values result from the involvement of high-frequency intramolecular vibrational modes in the non-radiative decay process; [8] since these electron-vibration couplings are an intrinsic feature of π-conjugated organic molecules, the two-state model implies that large non-radiative voltage losses should be expected for any D:A blend with CT states in the NIR region.

However, ΔV_{nr} values lower than 0.3 V have been recently reported for a number of high-efficiency non-fullerene-acceptor (NFA)-based OSC blends (PCE ~ 12 – 18%) with absorption bands extending to 900–1000 nm. [2, 6, 16, 21-22] This is highlighted in **Figure 1**, where we summarize the ΔV_{nr} values of more than 30 existing and new NFA-based OSC blends with small or negligible energy offsets (ΔE_{LE-CT}) between the lowest CT state and the lowest local-exciton (LE) state (see **Supplementary Figures S1** – **S4 and Tables S1** – **S2** for a description of materials and device characterizations). **Figure 1** indicates that the ΔV_{nr} values fluctuate in the range of 0.18–0.32 V and show no correlation with E_{CT}.

An important feature of these efficient NFA-based blends is that their energy offsets between either the ionization potentials (IP) or the electron affinities (EA) of the D and A components, which can be used as a first approximation to the ΔE_{LE-CT} values, are generally smaller than 0.2

eV. [6] This is in stark contrast to conventional fullerene-based blends where ΔE_{LE-CT} is usually in the range of 0.4–1 eV. [5, 23-26] The absence of any correlation between E_{CT} and ΔV_{nr} in NFA-based systems implies that the two-state model that lies at the origin of the energy-gap law is not valid for systems with small ΔE_{LE-CT} values. [9, 27] We, and others, previously proposed that a three-state model, which incorporates the hybridization between the LE and CT states, is required to rationalize the properties of state-of-the-art blends. [6, 9-10] However, while the involvement of hybridization makes the energy-gap-law dependence less strong, the three-state model cannot explain the absence of any correlation between E_{CT} and ΔV_{nr}, as experimentally observed in Figure 1. In reality, a key feature is that, since the CT and LE states are close or even resonant in energy, the impact of the thermal population of the LE state, a feature commonly neglected, [6, 10] should be considered.

Here, to describe the luminescence properties of D:A blends, we develop a three-state dynamic vibronic model that incorporates both the CT-LE hybridization and the thermal population of the states. Then, combining the three-state-based simulations with temperature-dependent electroluminescence measurements performed on a number of NFA-based blends, we are able to derive the essential electronic-structure parameters of the blends (*i.e.*, the ΔE_{LE-CT} energy offsets and the LE-CT electronic couplings $t_{LE\text{-}CT}$) and to establish the relationships among these parameters and ΔV_{nr}. Our results provide a *unified description* of ΔV_{nr} in OSCs and rationalize the low ΔV_{nr} values found in NFA-based blends with small energy offsets, as due to hybridization of the CT state with the highly emissive LE state and thermal population of the LE state. The critical message is that it is *the luminescence properties of the pristine low-optical-gap material that define the value of* ΔV_{nr} *in the OSC active layer*.

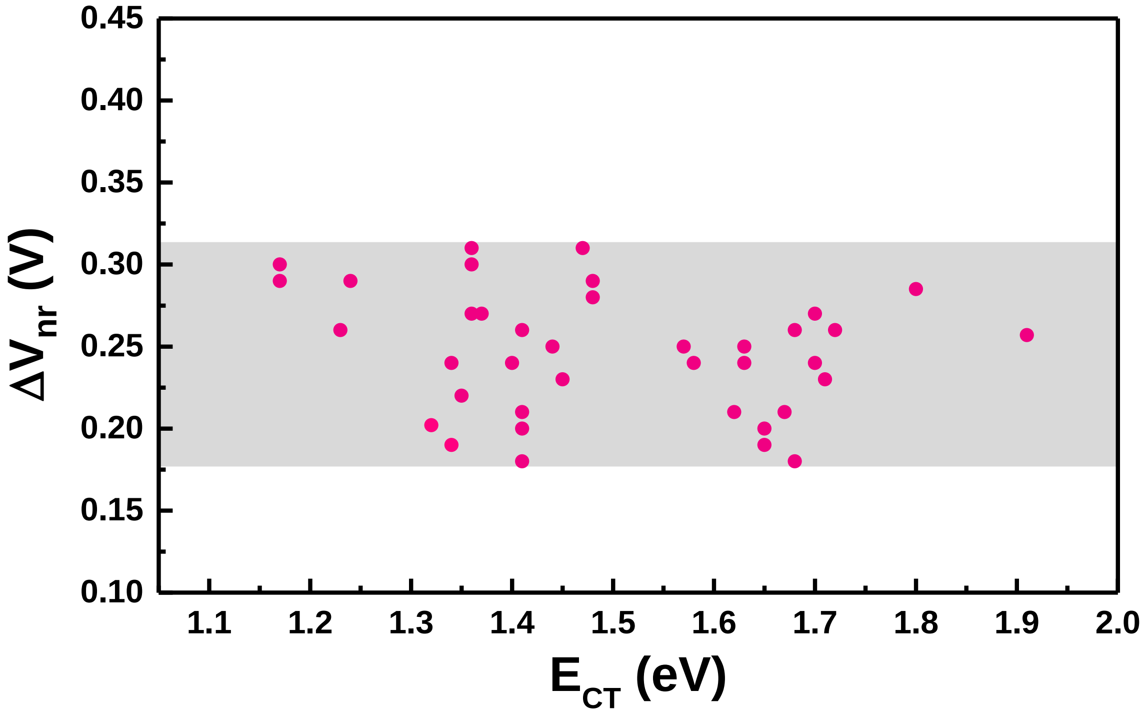

Figure 1. Non-radiative voltage losses (ΔV_{nr}) versus energies of interfacial CT states (E_{CT}). E_{CT} is estimated as the crossing point between the normalized photovoltaic EQE (EQE_{PV}) and EL spectra for the NFA-based blends with small or negligible ΔE_{LE-CT} values (see **Supplementary Figure S5**). The device ΔV_{nr} values are determined by two complementary approaches: (1) they are directly obtained from Equation 1 by measuring the device EQE_{EL} values; and (2) when the spectral range of the emission is deep into the infrared, they are estimated via (V_{OC}^{rad}- V_{OC}), where V_{OC}^{rad} is the maximum V_{OC} of a device assuming that recombination is purely radiative (see **Supplementary Table S2**).

Results and Discussion

The potential energy surfaces of the diabatic (*i.e.*, pure, non-electronically coupled) G, CT, and LE states involved in the three-state model are shown in **Figure 2A**. Switching on the electronic coupling t_{LE-CT} between the LE and CT states leads to the adiabatic (hybridized) states, which can be expressed as a superposition of the diabatic states (a comparison of diabatic and adiabatic states is shown in **Supplementary Figure S6**). The vibronic states related to the adiabatic potential energy surfaces (obtained from the solutions of the vibronic Hamiltonian Eq. (3) in the "Methods" section), which are involved in the actual electronic transitions, are shown as horizontal lines in **Figure 2A.** The emission spectra are determined by the electronic transitions from CT- and LE-dominant vibronic states (horizontal lines above the CT potential energy curve) to the lowest vibronic state (denoted as ν=0) (**Figure 2A**). The lineshapes and intensities of the optical emission spectra depend on the degree of CT-LE hybridization of the vibronic states (mainly governed by the $\Delta \mathrm{E}_{\mathrm{LE-CT}}$ energy offset and the $\mathrm{t}_{\mathrm{LE-CT}}$ electronic coupling) and on their thermal populations.

To assess the respective roles of CT-LE hybridization and thermal population, it is useful to consider first a low-temperature case for which only the lowest CT vibronic state is thermally populated. **Figure 2B** shows the calculated emission spectra at 30 K for $\Delta \mathrm{E}_{\mathrm{LE-CT}}$ = 250 meV as a function of $\mathrm{t}_{\mathrm{LE-CT}}$ values in the range of 1–50 meV (see **Supplementary Table S3** for a complete list of parameters and **Supplementary Figure S7** for additional results as a function of $\Delta \mathrm{E}_{\mathrm{LE-CT}}$). **Figure 2B** shows that an increase in $\mathrm{t}_{\mathrm{LE-CT}}$ leads to an increase in the CT-type emission intensity without any significant effect on the band shape; this evolution is the result of the hybridization of the weakly emissive CT state with a highly emissive LE state, an effect referred to as intensity borrowing. [28] Interestingly, even in the case where the CT state is dark, the CT-LE hybridization can still result in a CT-type emission band, see the dashed line in **Figure 2B**. The results obtained with the same set of parameters but at room temperature are shown in **Figure**

2C. For small $\mathrm{t_{LE-CT}}$, the emission becomes dominated by electronic transitions from thermally populated LE vibronic states; the overall spectrum resembles that of the pure donor or acceptor material. For large $\mathrm{t_{LE-CT}}$ values (*i.e.*, strong CT-LE hybridization), the spectral lineshape transforms back from LE-type to CT-type. For intermediate hybridization cases, both LE-type and CT-type transitions contribute to the spectral lineshape. These results underline that there exists a close interplay between the hybridization and thermal population effects on the spectral lineshape.

In order to shed more light on the thermal population effect, we measured the temperature dependence of the electroluminescence spectra of several selected D:A blends. The spectra of the PBDT-TS1:SF-$\mathrm{PDI_2}$ blend (see the chemical structures in **Supplementary Figure S1**) and of the pristine PBDT-TS1 polymer measured at 295 K are shown in **Figure 2D** along with the three-state model results**,** while the temperature-dependent spectra of the PBDT-TS1:SF-$\mathrm{PDI_2}$ blend are given in **Figure 2E**. The comparison between the blend and polymer spectra (**Figure 2D**) suggests that the high-energy emission shoulder of the blend corresponds to the polymer LE emission, and the main peak, to emission from the CT state. Indeed, **Figure 2E** indicates that with decreasing temperature the relative intensity of the high-energy shoulder gradually decreases and eventually disappears at low temperature. As seen from **Figure 2D,** the experimental spectrum of the blend can be very well simulated when considering $\mathrm{t_{LE-CT}}$ = 40 meV and $\Delta\mathrm{E_{LE-CT}}$ =150 meV.

We note that the simulation results are sensitive to the choice of the microscopic parameters (see **Supplementary Figure S8)**. To demonstrate the reliability of the derived microscopic parameters, we computed the temperature-dependent spectra based on the parameters obtained from the room-temperature simulation. The comparison of **Figures 2E** and **2F** highlights the very good qualitative agreement between the experimental and modelling results (more details are given in **Supplementary Figure S9**). A similar temperature dependence of the emission lineshapes is observed for other D:A systems (see **Supplementary Figure S10**).

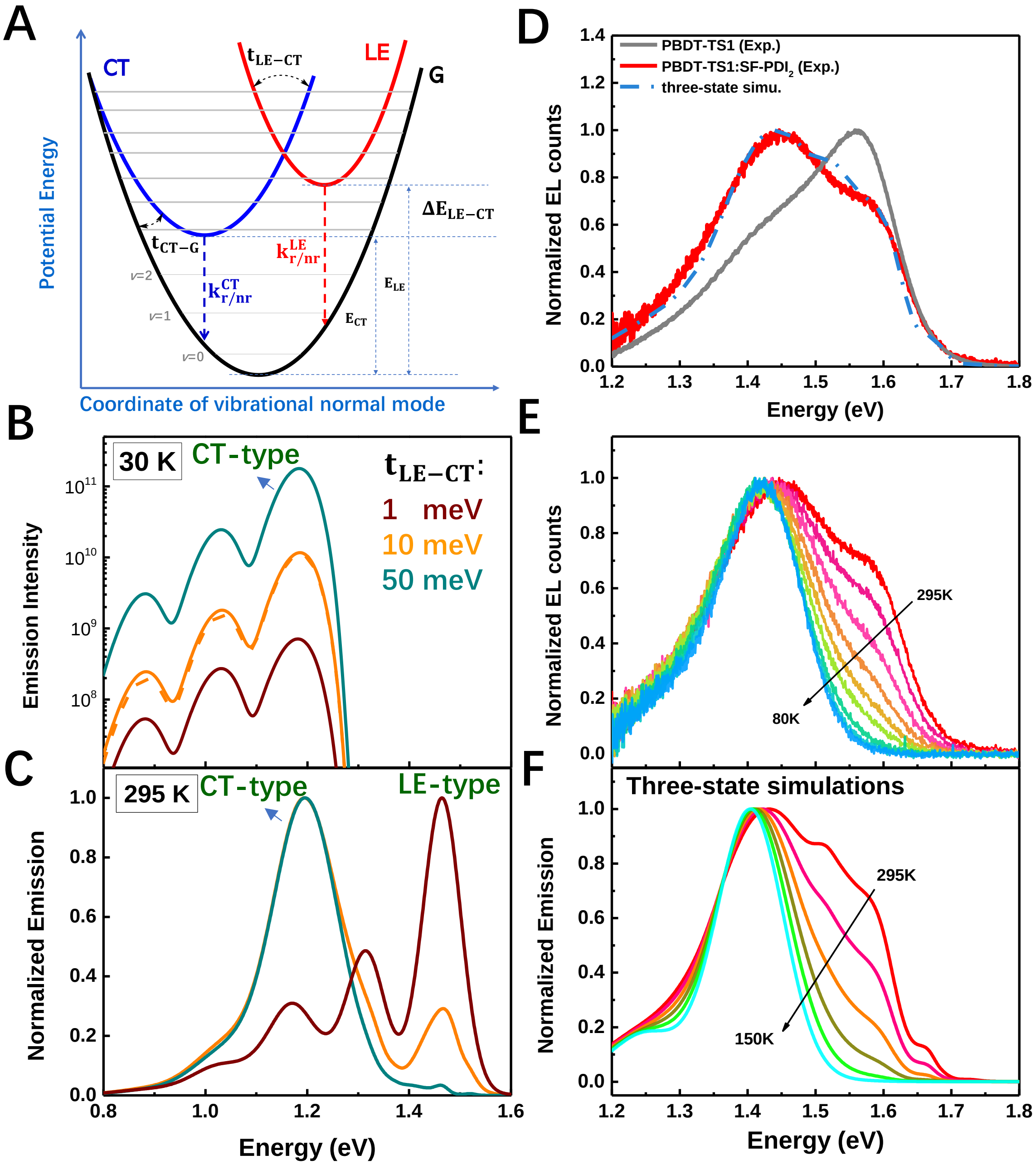

Figure 2. Emission spectral lineshapes of D:A blends as a function of electronic coupling $\mathbf{t_{LE-CT}}$. A. Schematic diagram of the potential energy curves for the G (black), CT (blue), and LE (red) diabatic states. $E_{LE/CT}$ denotes the relaxed excitation energy of the LE/CT state; t_{CT-G} and

t_{LE-CT} represent the electronic couplings of the CT state with the G state and LE state, respectively. The dashed blue and red lines illustrate the radiative and non-radiative decay rates of the diabatic CT and LE states. The horizontal gray lines denote the vibronic levels of the hybrid state. **B and C.** Spectral lineshapes calculated at 30 K (B) and 295 K (C) as a function of the t_{LE-CT} value, 1 meV (brown), 10 meV (orange), or 50 meV (indigo), via the three-state model with ΔE_{LE-CT}=250 meV. In (B), taking the case of t_{LE-CT}=10 meV as an example, we also provide spectrum calculated when the CT state is dark (the dashed line). **D.** Experimental emission spectra (at 295 K) of the PBDT-TS1:SF-PDI$_2$ blend (red solid line) and the pristine PBDT-TS1 film (gray solid line). The sky-blue dash-dotted line is the simulated spectral lineshape of the blend via the three-state model with $t_{LE-CT} =$ 40 meV and $\Delta E_{LE-CT} =$ 150 meV. **E** and **F**. Temperature dependent emission of PBDT-TS1:SF-PDI$_2$: (E) by experimental spectra and (F) their three-state simulations.

We now turn to the discussion of the effect that ΔE_{LE-CT} has on the blend emission spectra. We use a t_{LE-CT} value of 10 meV (a representative value for OSC active layers) and vary ΔE_{LE-CT} over a wide range at room temperature (see **Figure 3A**). For a large ΔE_{LE-CT} value (*e.g.*, 500 meV), only the CT-type emission peak is observed. When ΔE_{LE-CT} decreases to 250 meV, an LE-type emission peak appears in addition to the CT-type emission peak, due to the enhanced thermal population of the highly emissive LE vibronic states; with ΔE_{LE-CT} further reduced to or below 125 meV, the emission spectrum of the blend is dominated by transitions from the LE state.

These theoretical results are fully supported by the experimental EL spectra measured in blends based on the PBDT-TS1 polymer donor, as the low-optical-gap material, and five NFAs, namely di-PDI, TPH-Se, SF-PDI$_2$, T2 and IDFBR (see the chemical structures in **Supplementary Figure S1)**. In these blends, the $E_{EA_A-EA_D}$ offsets between the electron affinities (EAs) of PBDT-TS1 and the NFAs (which can be used as a first approximation to ΔE_{LE-CT}), as estimated from cyclic-voltammetry (CV) measurements, gradually decrease from 290 to 50 meV (see

Supplementary Figure S11 and Table S4). As shown in **Figure 3B**, with the reduction of the $\mathrm{E}_{\mathrm{EA_A - EA_D}}$ offset, the evolution of the spectral lineshapes can be very well reproduced by the three-state simulations (the electronic-structure parameters extracted from the simulations are listed in **Supplementary Table S5)**. Similar evolutions of the spectral lineshapes are observed in other D:A blends, such as the ITIC- and Y6-based blends (see **Supplementary Figure S12**). The derived microscopic parameters were then used to calculate the radiative and non-radiative recombination rates ($\mathrm{k_r}$ and $\mathrm{k_{nr}}$) of these blends and ultimately estimate the $\Delta \mathrm{V_{nr}}$ values (for computational details, see the "Methods" section). The $\Delta \mathrm{V_{nr}}$ values calculated for the PBDT-TS1 based systems are found to be in very good agreement with the experimental data (see **Supplementary Table S5**).

It is worth noting that, in the case of the PBDT-TS1:IDFBR blend that has a small energy offset (~ 50 meV), the spectral lineshape of the blend and its temperature dependence are nearly identical to those of pristine PBDT-TS1 (see **Figures 3C and 3D**), as is also the case in other blend materials with small $\Delta \mathrm{E_{LE-CT}}$ (**Supplementary Figure S13**). Once again, these results are in line with our three-state vibronic model: When the CT and LE states are close in energy, as a result of its significant thermal population, the PBDT-TS1 LE state dominates the blend emission.

Thus, our experimental and theoretical data demonstrate that the three-state vibronic model provides a reliable description of electronic transitions in D:A blends. In addition, our results underline that the combination of vibronic simulations with electroluminescence measurements represents a powerful tool to estimate the microscopic parameters relevant to the charge recombination processes in D:A blends.

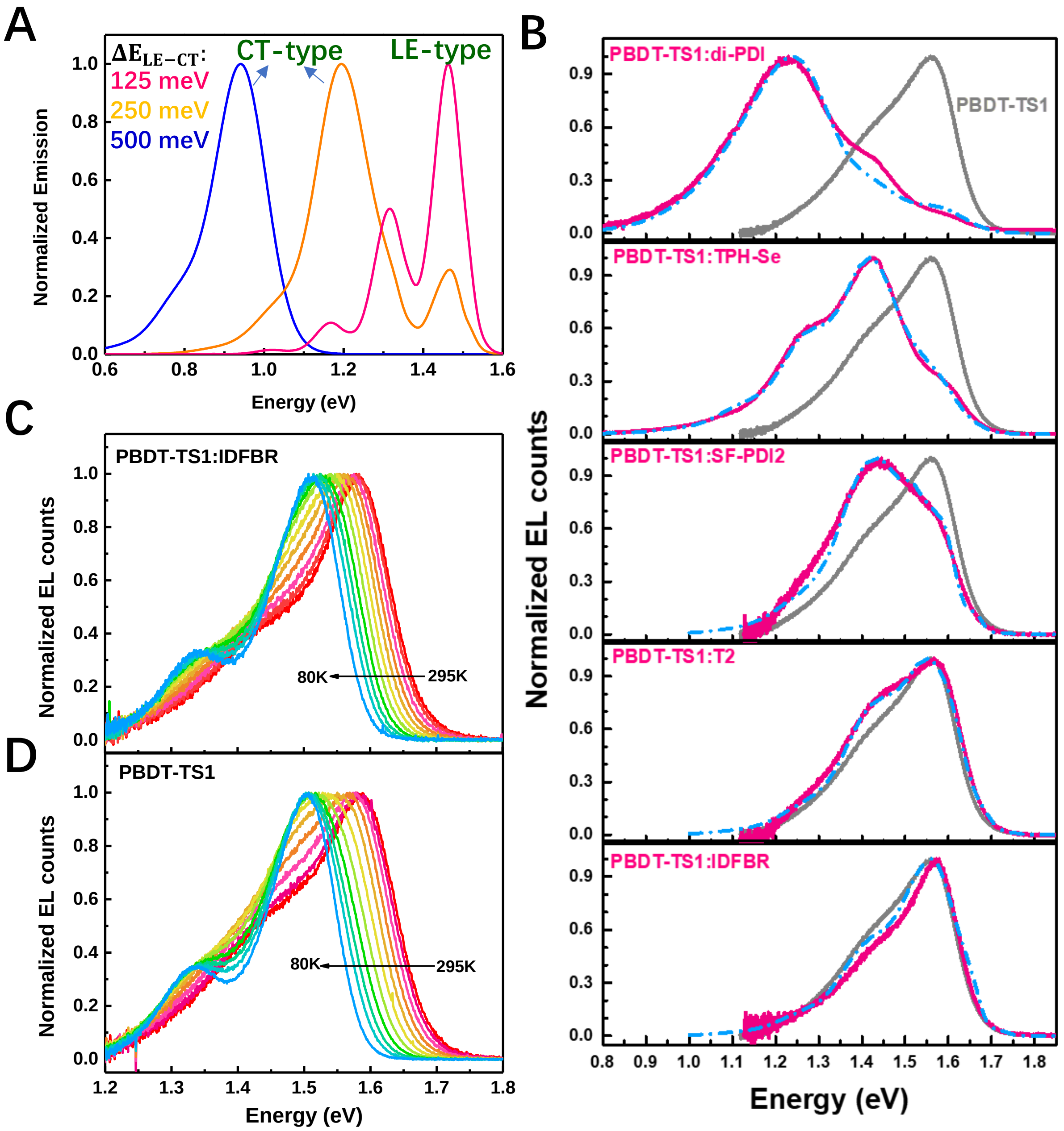

Figure 3. Emission spectral lineshapes of D:A blends as a function of the energy offset ΔE_{LE-CT}. A. Spectral lineshapes calculated at 295 K for D:A blends as a function of ΔE_{LE-CT} [500 meV (blue), 250 meV (orange), and 125 meV (pink)], via the three-state model with t_{LE-CT}=10 meV. Here, E_{LE} is fixed to 1.5 eV; ΔE_{LE-CT} is tuned by changing the E_{CT} values. **B.** Experimental emission spectra at 295 K of the PBDT-TS1 based blends (pink solid line) and the pristine PBDT-TS1 film (gray solid line). The sky-blue dash-dotted lines represent the spectra simulated via the three-state model; our procedure is first to simulate the emission spectrum of pristine PBDT-TS1 to extract the relevant electronic-structure parameters (such as E_{LE}, the vibronic coupling constants, and the vibrational frequencies) of the LE state; then, based on these

extracted parameters for the LE state, the emission spectra of the blends are simulated. **C** and **D**. Experimental temperature dependent emission spectra for PBDT-TS1:IDFBR (C) and pristine PBDT-TS1 (D).

Having demonstrated the reliability of the three-state model in simulating emission spectra, we now use this model to establish the relationships among ΔV_{nr} and the microscopic parameters. The results depend on the radiative and non-radiative decay rates of the CT (k_r^{CT} and k_{nr}^{CT}) and LE (k_r^{LE} and k_{nr}^{LE}) states. The dependences of k_r, k_{nr}, and ΔV_{nr} on the ΔE_{LE-CT} and t_{LE-CT} values are illustrated in **Figures 4A and 4B. Figure 4A** shows that, for large and intermediate ΔE_{LE-CT} values, the CT-LE hybridization has a strong effect on the radiative recombination rate of those D:A blends that have weak or moderate electronic couplings between the G and CT states (which is the case in most blends [29-30]); this comes from the fact that $k_r^{LE} \gg k_r^{CT}$. For instance, for a slow k_r^{CT} rate of 10^2 s^{-1}, even a weak CT-LE hybridization would increase k_r to 10^5-10^6 s^{-1}, a value typically found in D:A blends [31-33]. This finding suggests that the electronic hybridization effect plays a much more significant role in D:A blends than what has been commonly assumed. In contrast, the CT-LE hybridization has little effect on the blend k_{nr} value since the non-radiative rate from the LE state is much smaller than that from the CT state ($k_{nr}^{LE} \ll k_{nr}^{CT}$). It is only when E_{CT} increases and leads to a small ΔE_{LE-CT}, that hybridization starts to affect the non-radiative recombination rate of the blend; this is a result of the exponential dependence of k_{nr}^{CT} on E_{CT}, which then makes k_{nr}^{CT} smaller than k_{nr}^{LE}. At very small ΔE_{LE-CT} values, both radiative and non-radiative rates are dominated by the thermal population of the LE state, irrespective of the t_{LE-CT} values. We also note that an increase in the electronic coupling between the CT and G states can weaken the effects due to CT-LE hybridization and thermal population of the LE state on the radiative and non-radiative recombination rates of the blends (**Supplementary Figure S14**).

Figure 4B illustrates that $\Delta \mathrm{V}_{\mathrm{nr}}$ generally displays a linear-like dependence on $\Delta \mathrm{E}_{\mathrm{LE-CT}}$, even upon LE-CT hybridization. It is only when $\Delta \mathrm{E}_{\mathrm{LE-CT}}$ is reduced below 0.1 eV that, as a result of an increase in the thermal population of the LE state, a deviation from the linear dependence is observed; importantly, as $\Delta \mathrm{E}_{\mathrm{LE-CT}}$ vanishes, $\Delta \mathrm{V}_{\mathrm{nr}}$ experiences a major reduction and approaches the $\Delta \mathrm{V}_{\mathrm{nr}}$ value found in the pristine low-optical-gap material. This point is fully confirmed by the experimental data obtained from four sets of D:A blends based on Y6, ITIC, PBDT-TS1, and IEICO-4F, see **Figure 4C**. Thus, our model underlines that the lowest value achievable for $\Delta \mathrm{V}_{\mathrm{nr}}$ in a blend is determined by the photo-luminescence quantum yield (PLQY) of the low-optical-gap (D or A) material.

For the sake of completeness, we note that we have focused here on D:A blends suitable for high-performance OSCs, *i.e.*, those with LE absorption bands extending into the 900–1000 nm region. According to our model, in the case of blends with very high LE-state energies, in which case the CT-state energies can be > 2.0 eV, the $\mathrm{k}_{\mathrm{nr}}^{\mathrm{CT}}$ value becomes vanishingly small; as a result, small $\Delta \mathrm{V}_{\mathrm{nr}}$ values can also be obtained when $\Delta \mathrm{E}_{\mathrm{LE-CT}}$ is large, as experimentally observed in several D:A blends with high CT-state energies. [21]

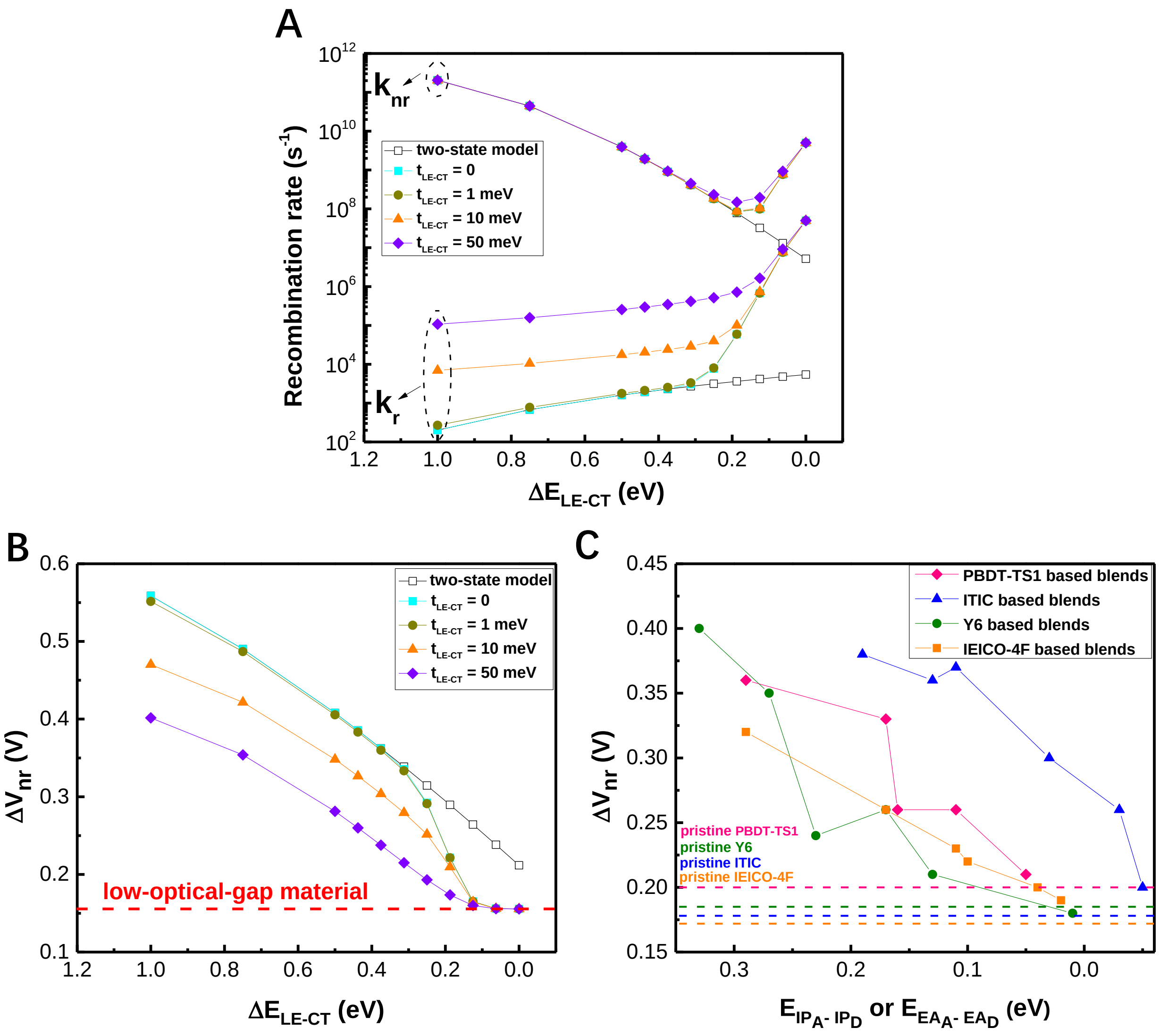

Figure 4. Non-radiative voltage losses as a function of ΔE_{LE-CT} and t_{LE-CT}. A. Radiative and non-radiative recombination rates (k_r and k_{nr}) calculated (at 295 K) as a function of ΔE_{LE-CT} and t_{LE-CT}. Here, E_{LE} is fixed to 1.5 eV; ΔE_{LE-CT} is tuned by changing the E_{CT} values. According to earlier experimental data, [6] the radiative and non-radiative decay rates (k_r^{LE} and k_{nr}^{LE}) for the LE state on the low-optical-gap material are fixed to 1×10^8 s^{-1} and 1×10^{10} s^{-1}, respectively, corresponding to a moderate value (1%) of photoluminescence quantum yield (PLQY). **B.** Calculated ΔV_{nr} as a function of ΔE_{LE-CT} and t_{LE-CT}. Based on the fixed k_r^{LE} and k_{nr}^{LE} values for the LE state, the ΔV_{nr} value of a device based on the pristine low-optical-gap material corresponds to ~ 0.16 V (red dashed line). Enhancing the PLQY of the low-optical-gap material further reduces the lowest value achievable for ΔV_{nr} in a blend (**Supplementary Figure S15**). **C.** Measured ΔV_{nr} as a function of the $E_{EA_A-EA_D}$ offset for the PBDT-TS1 based blends or $E_{IP_A-IP_D}$ for the ITIC, Y6, and IEICO-4F based blends. Here, all the experimental data related to IEICO-4F are obtained from the literature.[34] Pink, green, blue, and orange dashed lines denote

the measured ΔV_{nr} values of devices based on pristine PBDT-TS1 (0.2 V), Y6 (0.185 V [34]), ITIC (0.178 V [35]), and IEICO-4F (0.172 [34]) films, respectively.

In order to rationalize the experimental observations shown in **Figure 1,** we simulated the dependence of ΔV_{nr} on E_{CT} for a series of D:A systems, see **Figures 5A** and **5B.** For large ΔE_{LE-CT} values (taken randomly in the range of 0.4-1.0 eV and assuming a random distribution of t_{LE-CT} in the range of 1-50 meV), ΔV_{nr} follows a linear dependence on E_{CT}, see **Figure 5A**, which is consistent with the experimental data of Benduhn *et al.* derived for fullerene-based blends; [8] these experimental data show a significant scattering that, according to our results, can be in part attributed to different degrees of hybridization. Interestingly, the deviation from the linear relation, which appears for $E_{CT} > 1.6$ eV and is due to a transition to the case where $k_{nr}^{LE} \sim k_{nr}^{CT}$, is in line with the results obtained by Ullbrich *et al.* for D:A complexes with high PLQY. [21] For small ΔE_{LE-CT} values (lower than 0.1 eV), a small dependence of ΔV_{nr} on E_{CT} is observed in the case of E_{CT} values smaller than a threshold value; above threshold, ΔV_{nr} becomes independent of E_{CT}, see **Figure 5B**. We note that the data shown in **Figure 5B** were obtained by assuming a single set of k_r^{LE} and k_{nr}^{LE} values; in reality, different donor and acceptor materials have different k_r^{LE} and k_{nr}^{LE} values and thus different PLQY values, hence explaining the distribution in the ΔV_{nr} values shown in **Figure 1.**

As such, our results in **Figure 5B** rationalize the absence of any correlation between E_{CT} and ΔV_{nr} in **Figure 1**. We also note that this feature is not unique to NFA-based blends. The absence of a ΔV_{nr} *vs.* E_{CT} correlation is, in fact, also observed in fullerene-based blends with CT-state energies approaching the lowest excited state (S_1) of fullerene derivatives (located at about 1.7 eV

[23]). [8] As seen from **Supplementary Figure S16**, the ΔV_{nr} values for $\Delta E_{LE-CT} < 0.3$ eV follow the same trend as for NFA blends. However, since singlet excitons in the fullerene derivatives are only weakly emissive, the LE-CT hybridization in this case would not contribute to small ΔV_{nr} values; this highlights once again the necessity of having LE states with high PLQY values.

The results discussed above indicate that in the case of large ΔE_{LE-CT} values (*i.e.*, > 0.4 eV), only the CT emission band appears. The intensity of this band is strongly affected by the CT-LE hybridization, which reduces ΔV_{nr} via intensity borrowing. In addition, in this case, ΔV_{nr} still has a linear dependence on E_{CT}. In the blends with small ΔE_{LE-CT} (*i.e.*, < 0.1 eV), the CT-LE hybridization and the thermal population of the LE state lead to high EQE_{EL} (*i.e.*, small ΔV_{nr}). We note that the role of the thermal population gradually increases as ΔE_{LE-CT} approaches zero. In this case, ΔV_{nr} in the blend converges to the value in the pristine low-optical-gap material.

The main message here is that it is critical to design high-PLQY donor and acceptor materials with complementary optical absorption bands extending into the NIR region. The largest EQE_{EL}value, 0.14%, reported to date in the literature [16] is obtained for PM6:Y11 blends and results in a ΔV_{nr} value of 0.17 V. The EQE_{EL} value in a Y11 neat film is 0.5%, [16] which suggests that there is still significant room for further decrease of the ΔV_{nr} value; for instance, the use of a comparable acceptor with an EQE_{EL} of 10% could decrease the blend ΔV_{nr} to 0.06 V, making the ΔV_{nr} values in OSCs close to those in the best inorganic devices. Recent results on NIR organic light-emitting diodes (OLEDs), in particular those based on neutral-radical and thermally activated delayed fluorescence emitters, point to the feasibility of this objective. [36-38] Interestingly, in order to obtain high-efficiency OLEDs based on D:A exciplexes, it was also suggested [39] to use highly luminescent donor and acceptor molecules. Overall, these aspects confirm for the case of OSCs as well the consideration (underlined earlier in the case of inorganic and perovskite solar cells) that “a great solar cell needs to be a great LED”. [40-42]

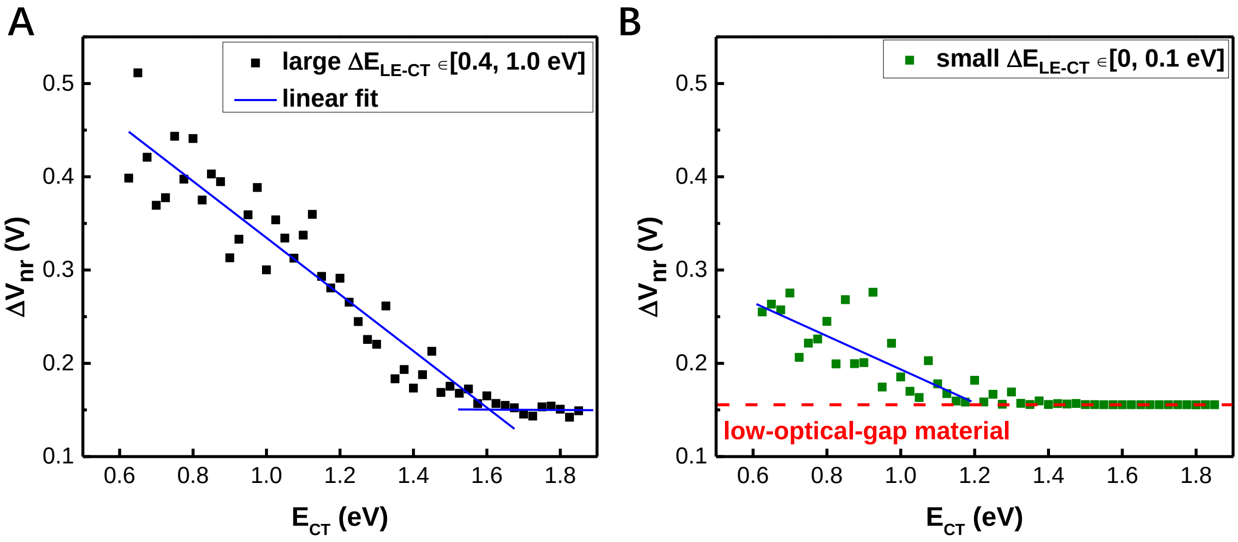

Figure 5. Unified description of non-radiative voltage losses. A and **B.** Calculated ΔV_{nr} as a function of E_{CT}, with ΔE_{LE-CT} randomly distributed in the range of [0.4–1.0 eV] for (A) or [0, 0.1eV] for (B), and t_{LE-CT} randomly distributed in the range of [1–50 meV].

Charge generation in devices based on NFA-based blends with small ΔE_{LE-CT} offsets is anticipated to involve a number of factors [6, 43-47] and a complete investigation of this topic is beyond the scope of the present contribution. However, to shed light on the relationship between ΔV_{nr} and charge-generation efficiencies, we plot in **Figure 6** the ratio $J_{SC}/J_{SC,SQ}$ (where J_{SC} is the short-circuit current density and $J_{SC,SQ}$, the current density evaluated from the Shockley-Queisser model [48]) as a function of ΔV_{nr} in OSC devices based on a wide range of blends. The key lesson from **Figure 6** is that charge-generation efficiencies and ΔV_{nr} values are not correlated. For D:A blends with a large ΔE_{LE-CT}, the significant driving force for exciton dissociation is expected to lead to efficient charge generation; however, this occurs at the expense of a large ΔV_{nr}, as reported for conventional material systems (*e.g.*, PTB7-Th:$PC_{71}BM$ shown in **Figure 6**). Efficient charge generation also is obtained in devices with small ΔE_{LE-CT} values, [45] which implies that low ΔV_{nr} values can be obtained without sacrificing charge generation. Benefitting from the rapid development of novel NFA materials, such as the Y-series acceptors, small ΔV_{nr} values (< 0.2 V) and highly efficient charge generations have been shown to be achieved simultaneously in NFA-based blends with small ΔE_{LE-CT}, as exemplified by the T1:Y6 and PTO2:Y6 systems reported here.

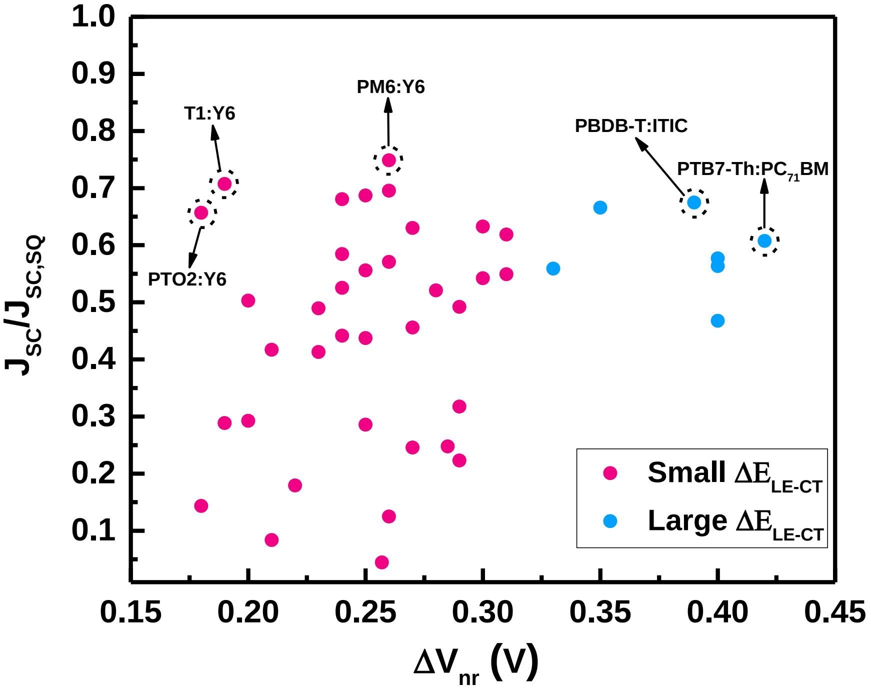

Figure 6. Charge generation efficiencies versus device ΔV_{nr}. J_{SC} is the short-circuit current density and $J_{SC,SQ}$, the current density evaluated from the Shockley-Queisser model. The corresponding device characteristics are given in Supplementary Table S6. The photovoltaic parameters of the PTO2:Y6 and T1:Y6 based OSCs are displayed in Supplementary Table S1 and Figure S2.

Conclusions

Our work has provided a unified description of the non-radiative voltage losses in organic solar cells. Our combined experimental and theoretical results demonstrate that low nonradiative voltage losses (ΔV_{nr}) are obtained in non-fullerene-acceptor based blends with a small ΔE_{LE-CT} offset, as a result of electronic hybridization of the highly emissive local-exciton (LE) state with the interfacial charge-transfer (CT) state and, more importantly, the thermal population of the LE state. We are able to explain, on the one hand, the energy-gap-law dependence found in fullerene-based blends, and, on the other hand, the absence of correlation between ΔV_{nr} and CT-state energy in state-of-the-art NFA-based blends. We find that the photoluminescence efficiencies of the pristine material components define the upper limit of the open-circuit voltage in organic solar cells. This is a very important point as it means that OSC active layers can be designed with optical gaps corresponding to the optimum value in the Shockley-Queisser limit, without having necessarily to pay a penalty in terms of the accessible voltage. Moreover, small ΔV_{nr} values (*e.g.*, < 0.2 eV) can be obtained without sacrificing the charge-generation efficiencies of the blends. We believe that what we have presented provides a clear guidance for the rational design of higher-efficiency OSC blends.

Methods

Materials: The conjugated materials studied in our work come either from companies or from groups involved in this work. IDFBR, SF-PDI2, di-PDI, IEICO-2F, O-IDTBR were purchased from 1-Materials Inc. SiOTIC-4F, COTIC-4F, PTO2, PM6, PBDB-T, PTB7-Th, PDCBT-2F, ITIC, COi8DFIC were purchased from Solar Materials Inc (Beijing). PBDT-TS1, PBDB-TCl, T1, IEICO-4F, T4, ITVffIC, J61, ITVfIC, J71, T2, TPH-Se, di-PDI were synthesized at the Chinese

Academy of Sciences. PTZ1, PTZ6, PBPD-Th were synthesized at the Soochow University. Y6 was synthesized at the Central South University.

Electrochemical oxidation potentials and electron affinities: Cyclic voltammetry (CV) measurements were performed on an Autolab PGSTAT10 with a three-electrode setup. Glassy carbon electrodes were used as the working electrode. A platinum wire was used as the counter electrode and a silver wire as pseudo-reference electrode. The reference electrode was calibrated with ferrocene. 0.1 M tetrabutylammonium hexafluorophosphate ($BuNPF_6$) in anhydrous acetonitrile solution was used as the supporting electrolyte. The polymers were drop-cast onto the working electrodes from corresponding chloroform solutions. During the measurements, the systems were bubbled with argon. CV was measured at a scan rate of 100 mV/s.

EL measurements: EL spectra were recorded by using an Andor spectrometer (a Shamrock sr-303i-B Spectrograph, coupled to a Newton EMCCD Si array detector cooled to -60 °C and an iDus InGaAs array detector cooled to -90 °C). An Oriel liquid light guide from Newport (Irvine, California, USA) was then connected to the entrance slit of the spectrometer and the other end was placed as close as possible to the active area of the samples. The system was wavelength calibrated by an argon lamp to a resolution better than 0.5 nm. The lineshapes of the recorded spectra were calibrated by an Optronic OL245 M standard spectral irradiance lamp. An external current/voltage source meter Keithley 2400 was connected to the photovoltaic devices comprising pure or blend films to inject electrons and holes into the devices. Acquisition was performed from 550 to 1000 nm with Si detector and from 900-1700 nm with InGaAs detector. The corresponding integration times were 60 seconds and several minutes, respectively. Temperature dependent EL measurements were conducted by mounting the devices in a liquid-helium cryostat. The temperature was monitored and controlled using a Lakeshore temperature monitor, with an Oxford Instruments ITC4 temperature controller controlling the heater.

EQE-EL measurement: The EQE-EL was recorded from a home-built system with a Hamamatsu silicon photodiode 1010B. A Keithley 2400 was used for supplying bias voltages and recording injected current, and a Keithley 485 was used for collecting the photo-current generated from the emitted photons of the samples.

Fabrication and characterization of bulk heterojunction and pristine devices: The device configurations were as followed: Indium tin oxide (ITO) / Poly(3,4-ethylenedioxythiophene) (PEDOT):poly(styrenesulfonate) (PSS) /active layer/ Poly(9,9-bis(3'-(N,N-dimethyl)-N-ethylammoinium-propyl-2,7-fluorene)-alt-2,7-(9,9-dioctylfluorene))dibromide (PFN-Br) /Al. The J-V curves were collected by using a Keithley 2400 Source Meter under AM1.5 illumination provided by a solar simulator (Model SS-50A, Photo Emission Tech., Inc.) with an intensity of 1000 W m^{-2}. The EQE spectra were recorded by an integrated quantum efficiency measurement system named QE-R3011 (Enli Technology Co. Ltd., Taiwan), which was calibrated with a crystalline silicon photovoltaic cell before use.

Three-state dynamic vibronic model: A hybrid state Ψ_{hybrid} is expressed as a linear superposition of the LE, CT , and G diabatic states ($|\Phi_{\mathrm{LE}}\rangle$, $|\Phi_{\mathrm{CT}}\rangle$, and $|\Phi_{\mathrm{G}}\rangle$), i.e.,

$$\Psi_{\mathrm{hybrid}} = \eta_{\mathrm{G}}(\mathrm{q})|\Phi_{\mathrm{G}}\rangle + \eta_{\mathrm{LE}}(\mathrm{q})|\Phi_{\mathrm{LE}}\rangle + \eta_{\mathrm{CT}}(\mathrm{q})|\Phi_{\mathrm{CT}}\rangle \tag{2}$$

where $\eta(\mathrm{q})$ denotes the expansion coefficients.

Following our earlier work, [9] the effective vibronic Hamiltonian matrix that accounts for linear electron-vibration couplings reads:

$$\mathbf{H}_{\mathbf{vibronic}} = \begin{pmatrix} \sum_{\mathrm{i}} \frac{\hbar\omega_{\mathrm{i}}}{2}(\mathrm{p}_{\mathrm{i}}^2 + \mathrm{q}_{\mathrm{i}}^2) & 0 & 0 \\ 0 & \sum_{\mathrm{i}} \frac{\hbar\omega_{\mathrm{i}}}{2}(\mathrm{p}_{\mathrm{i}}^2 + \mathrm{q}_{\mathrm{i}}^2) & 0 \\ 0 & 0 & \sum_{\mathrm{i}} \frac{\hbar\omega_{\mathrm{i}}}{2}(\mathrm{p}_{\mathrm{i}}^2 + \mathrm{q}_{\mathrm{i}}^2) \end{pmatrix}$$

$$+ \begin{pmatrix} \mathrm{E}_{\mathrm{LE}} + \lambda_{\mathrm{LE}} + \sum_{\mathrm{i}} \sqrt{2}\mathrm{g}_{\mathrm{i}}^{\mathrm{LE}}\hbar\omega_{\mathrm{i}}\mathrm{q}_{\mathrm{i}} & \mathrm{t}_{\mathrm{LE-CT}} & 0 \\ \mathrm{t}_{\mathrm{LE-CT}} & \mathrm{E}_{\mathrm{CT}} + \lambda_{\mathrm{CT}} + \sum_{\mathrm{i}} \sqrt{2}\mathrm{g}_{\mathrm{i}}^{\mathrm{CT}}\hbar\omega_{\mathrm{i}}\mathrm{q}_{\mathrm{i}} & \mathrm{t}_{\mathrm{CT-G}} \\ 0 & \mathrm{t}_{\mathrm{CT-G}} & 0 \end{pmatrix} \tag{3}$$

where E_{LE} and E_{CT} denote the relaxed excitation energies of the LE and CT states, respectively, see **Figure 2A**; $\mathrm{t}_{\mathrm{CT-G}}$ and $\mathrm{t}_{\mathrm{LE-CT}}$ denote the electronic couplings of the CT state with the G and LE states, respectively; p_{i} and q_{i} correspond to the dimensionless momentum and normal coordinate of the ith vibrational normal mode with energy $\hbar\omega_{\mathrm{i}}$, respectively; the relaxation energies of the CT and LE states (λ_{LE} and λ_{CT}) are directly related to the linear vibronic coupling constants (g_{i}) via $\lambda = \sum_{\mathrm{i}} \mathrm{g}_{\mathrm{i}}^2\hbar\omega_{\mathrm{i}}$. Here, our vibronic model includes two effective vibrational modes: a high-frequency (HF) vibration mode ($\hbar\omega_{\mathrm{HF}}$ = 0.15 eV (1200 cm^{-1})), typical of a carbon-carbon bond stretch, and a low-frequency (LF) vibration mode ($\hbar\omega_{\mathrm{LF}}$ = 12 meV (100 cm^{-1})), which represents rotations between intramolecular fragments as well as intermolecular motions.[9, 49]

The full dynamic solution of the vibronic Hamiltonian given by Eq. (3) can be obtained only numerically, by expanding the coefficients $\eta(\mathrm{q})$ in Eq. (2) in terms of the complete set of harmonic oscillator eigenfunctions, $|\chi_{\mathrm{m}}(\mathrm{q}_{\mathrm{i}})\rangle$:

$$\Psi_{\mathrm{hybrid};\alpha} = |\Phi_{\mathrm{G}}\rangle \sum_{\mathrm{m,n}} \mathrm{c}_{\mathrm{G;m,n}}^{\alpha} |\chi_{\mathrm{m}}(\mathrm{q}_1)\rangle\, |\chi_{\mathrm{n}}(\mathrm{q}_2)\rangle +$$

$$|\Phi_{\mathrm{LE}}\rangle \sum_{\mathrm{m'n'}} \mathrm{c}_{\mathrm{LE;m'n'}}^{\alpha} |\chi_{\mathrm{m'}}(\mathrm{q}_1)\rangle\, |\chi_{\mathrm{n'}}(\mathrm{q}_2)\rangle +$$

$$|\Phi_{\mathrm{CT}}\rangle \textstyle\sum_{\mathrm{m''n''}} \mathrm{c}_{\mathrm{CT;m''n''}}^{\alpha} |\chi_{\mathrm{m''}}(\mathrm{q}_1)\rangle\, |\chi_{\mathrm{n''}}(\mathrm{q}_2)\rangle \tag{4}$$

The αth adiabatic solution of the hybrid state is the superposition of the $|\Phi_{\mathrm{G}}\rangle$, $|\Phi_{\mathrm{LE}}\rangle$, and $|\Phi_{\mathrm{CT}}\rangle$ states where the c^{α} terms are the expansion coefficients. By using a finite but large enough number of vibrational functions (large m value), the eigenenergies and eigenfunctions of the vibronic Hamiltonian can be obtained with any desirable accuracy.

In order to easily and at the same time accurately simulate the optical emission properties of D:A pairs, we reasonably treat the electronic coupling between the CT and G states as perturbation, and then solve the eigen equation of the vibronic Hamiltonian (Eq. (3)). Based on the calculated eigenenergies E_α and eigenfunctions $\Psi_{\mathrm{hybrid},\alpha}$, the optical emission intensity $I_e(E)$ per donor/acceptor molecular pair at photon energy E is obtained from:

$$I_e(E) = E^3 \sum_\alpha f(E_\alpha) \sum_{m,n} \left|\langle \Psi_{\mathrm{hybrid};\alpha} | \vec{\mu} | \Psi_{G;m,n} \rangle\right|^2 \delta\left(E - \left(E_\alpha - E_{m,n}\right)\right) \tag{5}$$

where $f(E_\alpha)$ stands for the thermal (Boltzmann) population of the vibronic state E_α, $E_{m,n}$ denotes the sum of the energies of all the vibrational normal modes, and $\vec{\mu}$ is the dipole moment operator. In actual calculations, the delta function is replaced with a Gaussian broadening whose width is taken to be 100 cm^{-1} for all vibronic contributions, which is standard practice in vibronic theory. The transition dipole moment $\left|\langle \Psi_{\mathrm{hybrid};\alpha} | \vec{\mu} | \Psi_{G;m,n} \rangle\right|$ of each hybrid vibronic state is written as:

$$\left|\langle \Psi_{\mathrm{hybrid};\alpha} | \vec{\mu} | \Psi_{G;m,n} \rangle\right|^2 = \left|\vec{\mu}_{LE-G} c^{\alpha}_{LE;m,n} \delta_{m,m'} \delta_{n,n'}\right|^2 + \left|\vec{\mu}_{CT-G} c^{\alpha}_{CT;m,n} \delta_{m,m''} \delta_{n,n''}\right|^2 \tag{6}$$

Here, $\vec{\mu}_{LE-G}$ and $\vec{\mu}_{CT-G}$ denote the transition dipoles of the LE and CT states, respectively, and the latter is obtained via the Mulliken-Hush formula [50]:

$$|\vec{\mu}_{CT-G}| = \left|\frac{t_{CT-G}}{E_{CT}} e\vec{R}_{ET}\right| \tag{7}$$

where $\vec{R}_{ET}$ denotes the direction of interfacial electron [hole] transfer from donor [acceptor] to acceptor [donor], and e, the electron charge.

Theoretical estimation of the radiative and non-radiative recombination rates as well as the non-radiative voltage losses via the three-state model: As shown in Eq. (4), the adiabatic hybrid state is expressed as the superposition between the diabatic LE and CT states. To estimate the rates (k_r and k_{nr}) of the radiative and non-radiative recombinations of the hybrid state for D:A blends, the effects of the CT-LE hybridization and the thermal population of the hybrid state are considered in an effective way:

$$k_{r/nr} = \sum_\alpha f(E_\alpha) \sum_{m',n'} \left(c^{\alpha}_{LE;m',n'}\right)^2 \times k^{LE}_{r/nr} + \sum_\alpha f(E_\alpha) \sum_{m'',n''} {c^{\alpha}_{CT;m'',n''}}^2 \times k^{CT}_{r/nr} \tag{8}$$

where $k^{LE}_{r/nr}$ and $k^{CT}_{r/nr}$ denote the radiative/non-radiative recombination rates of the diabatic LE and CT states, respectively; $f(E_\alpha)$ stands for the thermal (Boltzmann) population of the hybrid vibronic state E_α; the $c^{\alpha}_{LE/CT}$ terms are the expansion coefficients in the αth solution of the vibronic state.

The radiative recombination rates (k^{CT}_r) of the diabatic CT state are estimated via the Einstein spontaneous-emission equation: [27]

$$k^{CT}_r = \frac{(E_{CT})^3 |\vec{\mu}_{CT-G}|^2}{3\pi\varepsilon_0 \hbar^4 c^3} \tag{9}$$

where $|\vec{\mu}_{CT-G}|$ denotes the transition dipole moment, related to the electronic coupling t_{CT-G} between the CT and G states via the Mulliken-Hush formula in Eq. (7); ε_0, the vacuum permittivity; $\hbar$, the reduced Planck constant; and c, the vacuum speed of light.

The non-radiative recombination rates (k_{nr}^{CT}) of the diabatic CT state are estimated via the Marcus-Levich-Jortner (MLJ) formula: [27]

$$k_{nr}^{CT} = \frac{2\pi}{\hbar}(t_{CT-G})^2 \frac{1}{\sqrt{4\pi(\lambda_{LF}+\lambda_{outer})k_BT+2\pi\sigma_s^2}} \sum_{n=0}^{\infty} \frac{e^{-S_{HF}}S_{HF}^n}{n!} \exp\left(-\frac{(\lambda_{LF}+\lambda_{outer}+n\hbar\omega-E_{CT})^2}{4(\lambda_{LF}+\lambda_{outer})k_BT+2\sigma_s^2}\right) \quad (10)$$

where λ_{LF} denotes the reorganization energy related to low-frequency (LF) classical vibrations; S_{HF}, the Huang–Rhys factor related to a high-frequency (HF) quantum vibration, with $S = g^2$ (with g, the linear vibronic coupling constant); λ_{outer}, the outer reorganization energy; and σ_s, the time-independent static energetic disorder.

Using these equations, in conjunction with Eq. (1), ΔV_{nr} in an OSC device is quantified via:

$$\Delta V_{nr} = -\frac{k_BT}{e}\ln\left(\vartheta \frac{k_r}{k_r+k_{nr}}\right) \quad (11)$$

where ϑ denotes the out-coupling factor of the device, which here is assumed to be 0.2.

Reporting Summary

Further information on experimental design is available in the Nature Research Reporting Summary linked to this article.

Data availability

The data that support the plots within this paper are available from the corresponding authors upon request.

Acknowledgments

The research in Linköping was supported by the Swedish Strategic Research Foundation through a Future Research Leader program to F.G. (FFL 18-0322), Swedish Research Council VR (Grant Nos. 2016-06146, 2018-05484, 2018-06048, and 2019-00677), the Swedish Energy Agency (Grant No. 43691-1), the Swedish Government Strategic Research Area in Materials Science on Functional Materials at Linköping University (Faculty Grant no. SFO-Mat-LiU #2009-00971); the work at Arizona was funded by the Department of the Navy, Office of Naval Research, under Award No. N00014-20-1-2110, and the University of Arizona. F.G. is a Wallenberg Academy Fellow, and O.I. is a Wallenberg Academy Scholar.

Author contributions

X.-K.C., D.Q., V.C., J.L.B., and F.G. conceived the project; X.-K.C. carried out all the theoretical simulations; D.Q. developed new blends; D.Q. made the devices and conducted the spectroscopy measurements together with Y.W.; T. K. and M.H. contributed to the measurements of the EL spectra, T.K., W.T., O.I., V.C., J.L.B., and F.G. contributed to the result analysis; D.Q. and J. Y.

conducted the CV measurements; H.Y., J.Y., M.Z., Y.Z., Y.L., and J.H. developed the donor and acceptor materials; Y.S. developed two of PBDT-TS1-based blends; X.-K.C., D.Q., V.C., J.L.B., and F.G. wrote the manuscript. All authors discussed the results and commented on the final manuscript.

Competing interests

The authors declare no competing interests.

References

1. National Renewable Energy Laboratory, Best research-cell efficiencies. https://www.nrel.gov/pv/assets/pdfs/best-research-cell-efficiencies.20200311.pdf **2020**.

2. Liu, Q.; Jiang, Y.; Jin, K.; Qin, J.; Xu, J.; Li, W.; Xiong, J.; Liu, J.; Xiao, Z.; Sun, K.; Yang, S.; Zhang, X.; Ding, L., 18% Efficiency organic solar cells. *Science Bulletin* **2020,** *65*, 272.

3. Hou, J.; Inganäs, O.; Friend, R. H.; Gao, F., Organic solar cells based on non-fullerene acceptors. *Nature Materials* **2018,** *17*, 119.

4. Menke, S. M.; Ran, N. A.; Bazan, G. C.; Friend, R. H., Understanding Energy Loss in Organic Solar Cells: Toward a New Efficiency Regime. *Joule* **2018,** *2*, 25.

5. Liu, X.; Rand, B. P.; Forrest, S. R., Engineering Charge-Transfer States for Efficient, Low-Energy-Loss Organic Photovoltaics. *Trends in Chemistry* **2019,** *1*, 815.

6. Qian, D.; Zheng, Z.; Yao, H.; Tress, W.; Hopper, T. R.; Chen, S.; Li, S.; Liu, J.; Chen, S.; Zhang, J.; Liu, X.-K.; Gao, B.; Ouyang, L.; Jin, Y.; Pozina, G.; Buyanova, I. A.; Chen, W. M.; Inganäs, O.; Coropceanu, V.; Bredas, J.-L.; Yan, H.; Hou, J.; Zhang, F.; Bakulin, A. A.; Gao, F., Design rules for minimizing voltage losses in high-efficiency organic solar cells. *Nature Materials* **2018,** *17*, 703.

7. Vandewal, K.; Tvingstedt, K.; Gadisa, A.; Inganäs, O.; Manca, J. V., On the origin of the open-circuit voltage of polymer–fullerene solar cells. *Nature Materials* **2009,** *8*, 904.

8. Benduhn, J.; Tvingstedt, K.; Piersimoni, F.; Ullbrich, S.; Fan, Y.; Tropiano, M.; McGarry, K. A.; Zeika, O.; Riede, M. K.; Douglas, C. J.; Barlow, S.; Marder, S. R.; Neher, D.; Spoltore, D.; Vandewal, K., Intrinsic non-radiative voltage losses in fullerene-based organic solar cells. *Nature Energy* **2017,** *2*, 17053.

9. Chen, X.-K.; Coropceanu, V.; Brédas, J.-L., Assessing the nature of the charge-transfer electronic states in organic solar cells. *Nature Communications* **2018,** *9*, 5295.

10. Eisner, F. D.; Azzouzi, M.; Fei, Z.; Hou, X.; Anthopoulos, T. D.; Dennis, T. J. S.; Heeney, M.; Nelson, J., Hybridization of Local Exciton and Charge-Transfer States Reduces Nonradiative Voltage Losses in Organic Solar Cells. *Journal of the American Chemical Society* **2019,** *141*, 6362.

11. Ran, N. A.; Love, J. A.; Takacs, C. J.; Sadhanala, A.; Beavers, J. K.; Collins, S. D.; Huang, Y.; Wang, M.; Friend, R. H.; Bazan, G. C.; Nguyen, T.-Q., Harvesting the Full Potential of Photons with Organic Solar Cells. *Advanced Materials* **2016,** *28*, 1482.

12. Ran, N. A.; Roland, S.; Love, J. A.; Savikhin, V.; Takacs, C. J.; Fu, Y.-T.; Li, H.; Coropceanu, V.; Liu, X.; Brédas, J.-L.; Bazan, G. C.; Toney, M. F.; Neher, D.; Nguyen, T.-Q., Impact of interfacial molecular orientation on radiative recombination and charge generation efficiency. *Nature Communications* **2017,** *8*, 79.

13. Ziffer, M. E.; Jo, S. B.; Zhong, H.; Ye, L.; Liu, H.; Lin, F.; Zhang, J.; Li, X.; Ade, H. W.; Jen, A. K. Y.; Ginger, D. S., Long-Lived, Non-Geminate, Radiative Recombination of Photogenerated Charges in a Polymer/Small-Molecule Acceptor Photovoltaic Blend. *Journal of the American Chemical Society* **2018,** *140*, 9996.

14. Liu, X.; Li, Y.; Ding, K.; Forrest, S., Energy Loss in Organic Photovoltaics: Nonfullerene Versus Fullerene Acceptors. *Physical Review Applied* **2019,** *11*, 024060.

15. Baran, D.; Kirchartz, T.; Wheeler, S.; Dimitrov, S.; Abdelsamie, M.; Gorman, J.; Ashraf, R. S.; Holliday, S.; Wadsworth, A.; Gasparini, N.; Kaienburg, P.; Yan, H.; Amassian, A.; Brabec, C. J.; Durrant, J. R.; McCulloch, I., Reduced voltage losses yield 10% efficient fullerene free organic solar cells with >1 V open circuit voltages. *Energy & Environmental Science* **2016,** *9*, 3783.

16. Liu, S.; Yuan, J.; Deng, W.; Luo, M.; Xie, Y.; Liang, Q.; Zou, Y.; He, Z.; Wu, H.; Cao, Y., High-efficiency organic solar cells with low non-radiative recombination loss and low energetic disorder. *Nature Photonics* **2020,** *14*, 300.

17. Green, M. A., Radiative efficiency of state-of-the-art photovoltaic cells. **2012,** *20*, 472.

18. Stranks, S. D., Nonradiative Losses in Metal Halide Perovskites. *ACS Energy Letters* **2017,** *2*, 1515.

19. Kirchartz, T.; Rau, U.; Kurth, M.; Mattheis, J.; Werner, J. H., Comparative study of electroluminescence from Cu(In,Ga)Se2 and Si solar cells. *Thin Solid Films* **2007,** *515*, 6238.

20. Rau, U., Reciprocity relation between photovoltaic quantum efficiency and electroluminescent emission of solar cells. *Physical Review B* **2007,** *76*, 085303.

21. Ullbrich, S.; Benduhn, J.; Jia, X.; Nikolis, V. C.; Tvingstedt, K.; Piersimoni, F.; Roland, S.; Liu, Y.; Wu, J.; Fischer, A.; Neher, D.; Reineke, S.; Spoltore, D.; Vandewal, K., Emissive and charge-generating donor–acceptor interfaces for organic optoelectronics with low voltage losses. *Nature Materials* **2019,** *18*, 459.

22. Cui, Y.; Yao, H.; Zhang, J.; Xian, K.; Zhang, T.; Hong, L.; Wang, Y.; Xu, Y.; Ma, K.; An, C.; He, C.; Wei, Z.; Gao, F.; Hou, J., Single-Junction Organic Photovoltaic Cells with Approaching 18% Efficiency. *Advanced Materials* **2020**, DOI: 10.1002/adma.201908205.

23. Faist, M. A.; Kirchartz, T.; Gong, W.; Ashraf, R. S.; McCulloch, I.; de Mello, J. C.; Ekins-Daukes, N. J.; Bradley, D. D. C.; Nelson, J., Competition between the Charge Transfer State and the Singlet States of Donor or Acceptor Limiting the Efficiency in Polymer:Fullerene Solar Cells. *Journal of the American Chemical Society* **2012,** *134*, 685.

24. Coffey, D. C.; Larson, B. W.; Hains, A. W.; Whitaker, J. B.; Kopidakis, N.; Boltalina, O. V.; Strauss, S. H.; Rumbles, G., An Optimal Driving Force for Converting Excitons into Free Carriers in Excitonic Solar Cells. *The Journal of Physical Chemistry C* **2012,** *116*, 8916.

25. Vandewal, K., Interfacial Charge Transfer States in Condensed Phase Systems. *Annual Review of Physical Chemistry* **2016,** *67*, 113.

26. Rand, B. P.; Burk, D. P.; Forrest, S. R., Offset energies at organic semiconductor heterojunctions and their influence on the open-circuit voltage of thin-film solar cells. *Physical Review B* **2007,** *75*, 115327.

27. Coropceanu, V.; Chen, X.-K.; Wang, T.; Zheng, Z.; Brédas, J.-L., Charge-transfer electronic states in organic solar cells. *Nature Reviews Materials* **2019,** *4*, 689.

28. Bixon, M.; Jortner, J.; Verhoeven, J. W., Lifetimes for Radiative Charge Recombination in Donor-Acceptor Molecules. *Journal of the American Chemical Society* **1994,** *116*, 7349.

29. Fu, Y.-T.; da Silva Filho, D. A.; Sini, G.; Asiri, A. M.; Aziz, S. G.; Risko, C.; Brédas, J.-L., Structure and Disorder in Squaraine–C60 Organic Solar Cells: A Theoretical Description of Molecular Packing and Electronic Coupling at the Donor–Acceptor Interface. *Advanced Functional Materials* **2014,** *24*, 3790.

30. Han, G.; Guo, Y.; Ma, X.; Yi, Y., Atomistic Insight Into Donor/Acceptor Interfaces in High-Efficiency Nonfullerene Organic Solar Cells. *Solar RRL* **2018,** *2*, 1800190.

31. Zheng, Z.; Tummala, N. R.; Wang, T.; Coropceanu, V.; Brédas, J.-L., Charge-Transfer States at Organic–Organic Interfaces: Impact of Static and Dynamic Disorders. *Advanced Energy Materials* **2019,** *9*, 1803926.

32. Zheng, Z.; Tummala, N. R.; Fu, Y.-T.; Coropceanu, V.; Brédas, J.-L., Charge-Transfer States in Organic Solar Cells: Understanding the Impact of Polarization, Delocalization, and Disorder. *ACS Applied Materials & Interfaces* **2017,** *9*, 18095.

33. Wang, T.; Brédas, J.-L., Organic Solar Cells Based on Non-fullerene Small-Molecule Acceptors: Impact of Substituent Position. *Matter* **2020,** *2*, 119.

34. Xie, Y.; Wang, W.; Huang, W.; Lin, F.; Li, T.; Liu, S.; Zhan, X.; Liang, Y.; Gao, C.; Wu, H.; Cao, Y., Assessing the energy offset at the electron donor/acceptor interface in organic solar cells through radiative efficiency measurements. *Energy & Environmental Science* **2019,** *12*, 3556.

35. Zhao, W.; Qian, D.; Zhang, S.; Li, S.; Inganäs, O.; Gao, F.; Hou, J., Fullerene-Free Polymer Solar Cells with over 11% Efficiency and Excellent Thermal Stability. *Advanced Materials* **2016,** *28*, 4734.

36. Zampetti, A.; Minotto, A.; Cacialli, F., Near-Infrared (NIR) Organic Light-Emitting Diodes (OLEDs): Challenges and Opportunities. *Advanced Functional Materials* **2019,** *29*, 1807623.

37. Kim, D.-H.; D'Aléo, A.; Chen, X.-K.; Sandanayaka, A. D. S.; Yao, D.; Zhao, L.; Komino, T.; Zaborova, E.; Canard, G.; Tsuchiya, Y.; Choi, E.; Wu, J. W.; Fages, F.; Brédas, J.-L.; Ribierre, J.-C.; Adachi, C., High-efficiency electroluminescence and amplified spontaneous emission from a thermally activated delayed fluorescent near-infrared emitter. *Nature Photonics* **2018,** *12*, 98.

38. Ai, X.; Evans, E. W.; Dong, S.; Gillett, A. J.; Guo, H.; Chen, Y.; Hele, T. J. H.; Friend, R. H.; Li, F., Efficient radical-based light-emitting diodes with doublet emission. *Nature* **2018,** *563*, 536.

39. Goushi, K.; Yoshida, K.; Sato, K.; Adachi, C., Organic light-emitting diodes employing efficient reverse intersystem crossing for triplet-to-singlet state conversion. *Nature Photonics* **2012,** *6*, 253.

40. Miller, O. D.; Yablonovitch, E.; Kurtz, S. R., Strong Internal and External Luminescence as Solar Cells Approach the Shockley–Queisser Limit. *IEEE Journal of Photovoltaics* **2012,** *2*, 303.

41. Pazos-Outón, L. M.; Szumilo, M.; Lamboll, R.; Richter, J. M.; Crespo-Quesada, M.; Abdi-Jalebi, M.; Beeson, H. J.; Vrućinić, M.; Alsari, M.; Snaith, H. J.; Ehrler, B.; Friend, R. H.; Deschler, F., Photon recycling in lead iodide perovskite solar cells. *Science* **2016,** *351*, 1430.

42. Yablonovitch, E., Lead halides join the top optoelectronic league. *Science* **2016,** *351*, 1401.

43. Perdigón-Toro, L.; Zhang, H.; Markina, A.; Yuan, J.; Hosseini, S. M.; Wolff, C. M.; Zuo, G.; Stolterfoht, M.; Zou, Y.; Gao, F.; Andrienko, D.; Shoaee, S.; Neher, D., Barrierless Free Charge Generation in the High-Performance PM6:Y6 Bulk Heterojunction Non-Fullerene Solar Cell. *Advanced Materials* **2020,** *32*, 1906763.

44. Karki, A.; Vollbrecht, J.; Dixon, A. L.; Schopp, N.; Schrock, M.; Reddy, G. N. M.; Nguyen, T.-Q., Understanding the High Performance of over 15% Efficiency in Single-Junction Bulk Heterojunction Organic Solar Cells. *Advanced Materials* **2019,** *31*, 1903868.

45. Zhong, Y.; Causa', M.; Moore, G. J.; Krauspe, P.; Xiao, B.; Günther, F.; Kublitski, J.; Shivhare, R.; Benduhn, J.; BarOr, E.; Mukherjee, S.; Yallum, K. M.; Réhault, J.; Mannsfeld, S. C. B.; Neher, D.; Richter, L. J.; DeLongchamp, D. M.; Ortmann, F.; Vandewal, K.; Zhou, E.; Banerji, N., Sub-picosecond charge-transfer at near-zero driving force in polymer:non-fullerene acceptor blends and bilayers. *Nature Communications* **2020,** *11*, 833.

46. Yao, H.; Cui, Y.; Qian, D.; Ponseca, C. S.; Honarfar, A.; Xu, Y.; Xin, J.; Chen, Z.; Hong, L.; Gao, B.; Yu, R.; Zu, Y.; Ma, W.; Chabera, P.; Pullerits, T.; Yartsev, A.; Gao, F.; Hou, J., 14.7% Efficiency Organic Photovoltaic Cells Enabled by Active Materials with a Large Electrostatic Potential Difference. *Journal of the American Chemical Society* **2019,** *141*, 7743.

47. Chow, P. C. Y.; Hinrichsen, T. F.; Chan, C. C. S.; Paleček, D.; Gillett, A.; Chen, S.; Zou, X.; Ma, C.; Zhang, G.; Yip, H.-L.; Wong, K. S.; Friend, R. H.; Yan, H.; Rao, A., Long-lived and disorder-free charge transfer states enable endothermic charge separation in efficient non-fullerene organic solar cells. *arXiv:2004.02487 [physics.app-ph]*.

48. Shockley, W.; Queisser, H. J., Detailed Balance Limit of Efficiency of p‐n Junction Solar Cells. *Journal of Applied Physics* **1961,** *32*, 510.

49. Kahle, F.-J.; Rudnick, A.; Bässler, H.; Köhler, A., How to interpret absorption and fluorescence spectra of charge transfer states in an organic solar cell. *Materials Horizons* **2018,** *5*, 837.

50. Creutz, C.; Newton, M. D.; Sutin, N., Metal—lingad and metal—metal coupling elements. *Journal of Photochemistry and Photobiology A: Chemistry* **1994,** *82*, 47.